

Shape descriptors to characterize the shoot of entire plant from multiple side views of a motorized depth sensor

Yann Chéné¹  · David Rousseau² · Étienne Belin¹ · Morgan Garbez³ · Gilles Galopin³ · François Chapeau-Blondeau¹

Received: 19 September 2013 / Revised: 22 March 2016 / Accepted: 23 March 2016 / Published online: 19 April 2016
© Springer-Verlag Berlin Heidelberg 2016

Abstract A low-cost depth camera recently introduced is synchronized with a specially devised low-cost motorized turntable. This results in a low-cost motorized depth sensor, able to provide a large number of registered side views, which is exploited here for the quantitative characterization of the shoots of entire plants. A set of four new shape descriptors of the shoots, constructed from the depth images on multiple side views of the shoots of plants, is proposed. The four descriptors quantify effective volume, multiscale organization, spatial symmetries and lacunarity of the plants. The four descriptors are here defined, validated on synthetic scenes with known properties, and then applied on nine different-looking real plants to illustrate their abilities for quantitative characterization and comparison. The resulting motorized depth sensor and associated image processing open new perspectives to various plant science applications including plant growth and architecture monitoring, plant response to stresses or the assessment of aesthetic parameters for ornamental plants.

Keywords Kinect · Depth image · Shape descriptor · Fractal · Plant shoots · Phenotyping

✉ Étienne Belin
etienne.belin@univ-angers.fr

- ¹ Laboratoire Angevin de Recherche en Ingénierie des Systèmes (LARIS), Université d'Angers, 62 avenue Notre Dame du Lac, 49000 Angers, France
- ² Université de Lyon, CREATIS, CNRS UMR 5220, INSERM U1044, Université Lyon 1, INSA-Lyon, 69621 Villeurbanne, France
- ³ Agrocampus Ouest, Centre d'Angers-Institut National d'Horticulture et du Paysage, UMR 1345 IRHS (Agrocampus Ouest, INRA, Université d'Angers), 2 rue Le Nôtre, 49045 Angers Cedex 01, France

1 Introduction

At different observation scales, plants (seedling, roots, entire plant) are formed of complex spatial structures. The non-destructive and noninvasive analysis of these structures and monitoring of their spatio-temporal evolutions is a topic of current interest for computer vision specially when applied to the domain of high-throughput phenotyping (see [1] for a recent review and see [2–4], for recent issues in this journal) where large populations of plants are to be characterized in relation to their environment and genotype. The shape analysis of the structures in the shoots of plants (leaflets, leaves, branches together with other organs) is challenging from conventional RGB imaging since in most cases the shoots of plants are globally homogenous in color. However, gazing at plants with other imaging sensors can help to overcome this challenge. Because of the discrete location of the leaves along the branching structure of the plants, contrast between leaves is likely to exist in their distinct relative distances to a camera. Following this idea, it has recently been shown that depth sensors, providing distance maps between the forefront of a scene and the imaging sensor, can be useful to the characterization of the structure of the shoots of entire plants [1, 5–17]. Various observation scales, including small plants [1], more structured shoots of entire plants [6, 7, 11–14] and canopy [5, 8–10, 15], have been analysed with depth cameras. Different technologies of depth sensors have been used: a laser scanner in [9, 10], time of flight cameras in [5, 11, 12], the stereovision in [6, 8, 16] or the structured lighting in [7, 13–15, 17]. Similarly to what has been undertaken in other fields of engineering [18], a comparison of some of these three-dimensional (3D) imaging technologies has recently been undertaken on the same plants [14]. Interestingly, it appears that the sensor used in [7, 13], the Microsoft Kinect sensor, although of very low cost is competitively applicable for the characterization

of a large variety of shoots of plants. In [13, 14], the segmentation of each individual leaf was performed with the Microsoft Kinect from indoor single top views of rosebushes or apple trees. In [7], such single top views of outdoor acquisitions with the same low-cost sensor were shown also valuable for the characterization of the ensemble of the shoots of artichoke and rubber trees. Although a top view already carries relevant information on the shoot structure, there are much more to be gained for a full characterization of the structure of the shoots if additional views can be acquired. In this article, we propose to extend the work of [7, 13, 14] in the direction of the characterization of the ensemble of the shoots from multiple acquisitions with a low-cost depth sensor coupled with a motorized turntable. As 3D full reconstruction of the shoots is sometimes a hard task owing to complexity of shoot spatial structures, we propose using depth images around the plant to characterize depth of the shoots of the plant.

The article is organized as follows: We first describe the acquisition system. Then, we propose shape descriptors devised to quantify traits of the shoots of entire plants from depth images. Such traits are specifically used by botanists to describe plants by sensorial attribute scores of ornamental plants assessed in 3D as recently published in [19]. For calibration purposes, we test our descriptors on synthetic scenes. We finally illustrate our new sensor on nine different-looking plants and discuss its relevance for different plant science applications.

2 Motorized depth sensor

The depth sensor of the Microsoft Kinect uses active triangulation to compute the depth of the forefront objects in a scene. This sensor measures 27.9 cm × 6.3 cm × 3.8 cm, weighs 1.36 kg and includes a motor to control its position. It is composed of an infrared (IR) light source and a CMOS sensor equipped with a bandpass IR filter. The IR light source is projected through a diffraction grid resulting in a pseudo-random speckle pattern of binary light dots. The neighbourhood of each light dot is unique. The depth image is then computed from differences between a reference speckle pattern obtained at a given distance and the speckle pattern viewed by the IR sensor. Each light dot is retrieved in the reference speckle pattern by an image correlation of a 9 × 9 window around the point due to its unique neighbourhood. Finally, the depth in each pixel is computed with a triangulation method. Use of the active triangulation results in a very low-cost depth sensor. Depth images are delivered with a resolution of 640 × 480 pixels at 30 frames per second with a field of view of 57° × 43°. Depth is coded on 11 bits with a precision of 1 cm at a distance of 2 m. The precision decreases quadratically with depth [20]. From our practical use of this depth sensor, the range of depth is 0.5–6 m. The

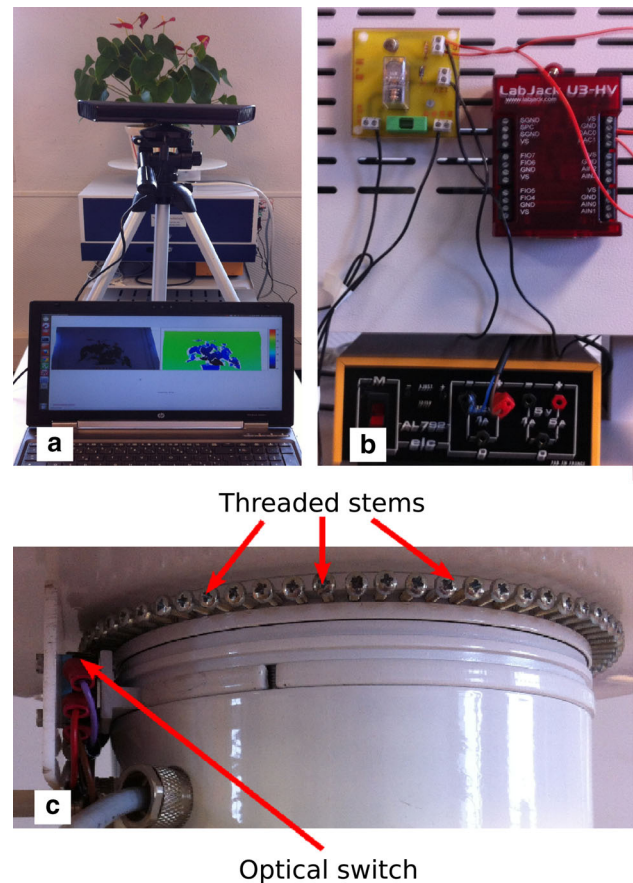


Fig. 1 A motorized depth sensor to characterize the depth of the shoots of entire plants. **a** Global view of the motorized depth sensor. **b** A LabJack system triggers the rotation by sending an electrical impulse to the rotating plate. **c** An optical switch detects the passing of the threaded stems and stops the rotation

synchronization of the Microsoft Kinect depth sensor with the rotation of a motorized turntable results in a motorized depth sensor displayed by Fig. 1a.

The turntable has been specifically devised and assembled with constraints of low cost and transportability. Synchronized with the depth sensor, it results in a motorized depth sensor which can acquire depth images of plants weighting up to 15 kg. Depth images are acquired every 5° for a total of 72 poses all around the plant. The rotation system has been realized so as to transform a continuous mode into a step-by-step mode every 5° at a low cost. A LabJack system [21], connected to a computer, triggers the rotation by sending an electrical impulse to the rotative system (see Fig. 1b). Threaded stems are placed at periodic intervals along the border of the rotating plate (see Fig. 1c). At each rotation, an optical switch detects the passing of a threaded stem and stops the rotation, the depth image acquisition is performed after a delay to avoid perturbing the image acquisition with movements from the shoots of the plant that would be induced by rotation. The motorized depth sensor is managed with an homemade Qt

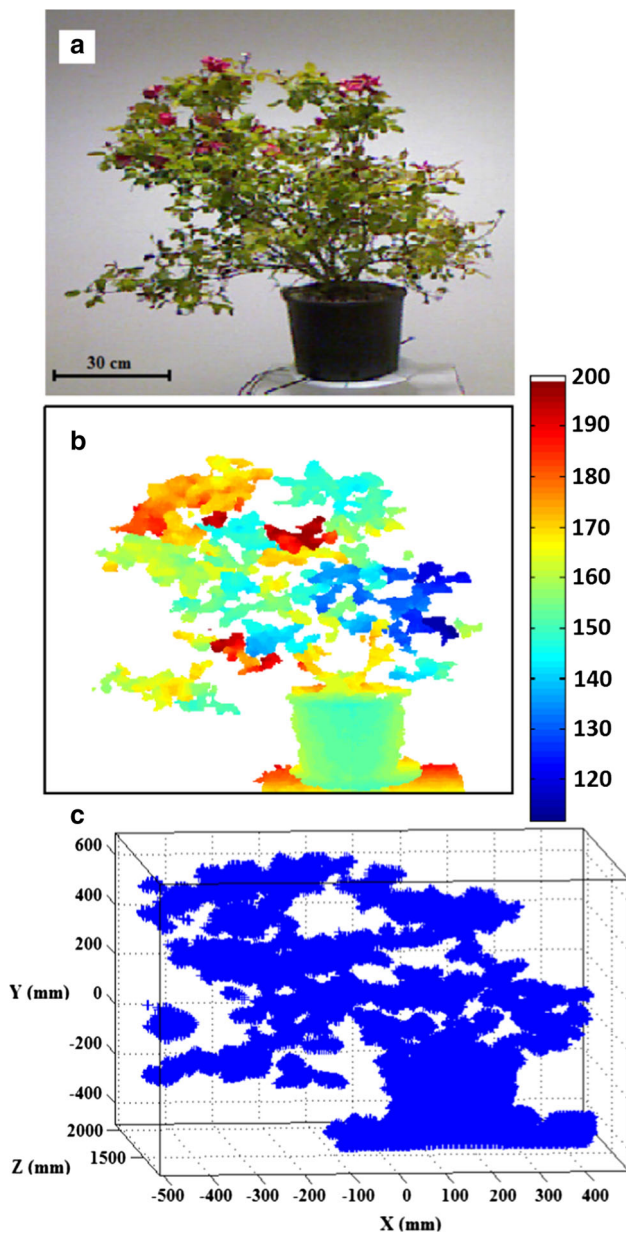


Fig. 2 Example of a plant characterized in its depth from acquisitions with the motorized depth sensor. **a** The RGB image of the plant (the given *scale bar* corresponds to the spatial resolution in the median plane of the pot). **b** Corresponding depth image (depth values are in cm). **c** Corresponding point cloud

[22] interface written in C++ language and based on OpenNI [23] drivers to acquire depth images of the Kinect Microsoft depth sensor. Figure 2 gives an example of a plant characterized in its depth with our motorized depth sensor.

3 Shape descriptors

A depth image provides in each pixel the depth of forefront points of the shoots of the plant (see Fig. 2b). From a known

formula [20], each pixel can be converted to a point, with 3D coordinates (X, Y, Z) expressed in metres, in a given 3D reference. The conversion of all points of the shoots of the plant results in a 2.5D representation of the shoots of the plant, called the point cloud (see Fig. 2c). Limits of this point cloud are the rectangular box with faces orthogonal to the coordinate axes (X, Y, Z) and passing through the two extreme coordinates found for the points in the cloud along each of the three axes (X, Y, Z) . In practice, the pot was withdrawn by a threshold on height because the plant tested was elongated enough so that extremely few pixels of the plant were found to be located at an altitude below the pot height. It would be possible to improve this procedure by detecting the conical shape of the pot in the point cloud for example using the RANSAC algorithm for conical shape present in the PCL library of C++ [24].

In this article, we introduce four new descriptors specially built for depth characterization of the shoots of the plant: the effective volume, the multiscale analysis (box counting and number of neighbours methods), the 3D symmetry (longitudinal, transverse and parallel symmetries) and the hole ratios. Independently extracted from each view of the plant, these descriptors are computed either from the depth map (hole ratios), from the point cloud (multiscale analysis and 3D symmetry), or from both representations (effective volume). In the sequel, we first describe the computation of the four new shape descriptors, and then we use synthetic scene with a known depth image and point cloud to validate the computation of each descriptor.

3.1 Effective volume

The real volume of a plant is the sum of volumes of all its single elements (stem and organs) and it can only be computed from the total 3D reconstruction of the plant. In this study, we do not reconstruct the plant. So we propose a new descriptor describing the space filled by the plant: the effective volume. In physics, an effective surface is the visible surface from a certain point of view. By analogy, the effective volume is the volume viewed from the depth sensor point of view.

This effective volume could be estimated, as in [7], from the volume of the convex hull that contains all the point cloud. However, this measurement is only based on coordinates of the convex hull vertices, so it is a global estimation of the effective volume. Here, to improve the effective volume measurement, we propose a new algorithm which compute the effective volume as the sum of local effective volumes. For each point i of the point cloud, the distance D_i is the difference between the maximum depth value in the point cloud and the depth value Z_i of the point i . So, we define the local effective volume of each point i of the point cloud as the product between the area of a local polygon around the point i with D_i . Figure 3 depicts the steps followed to find the local

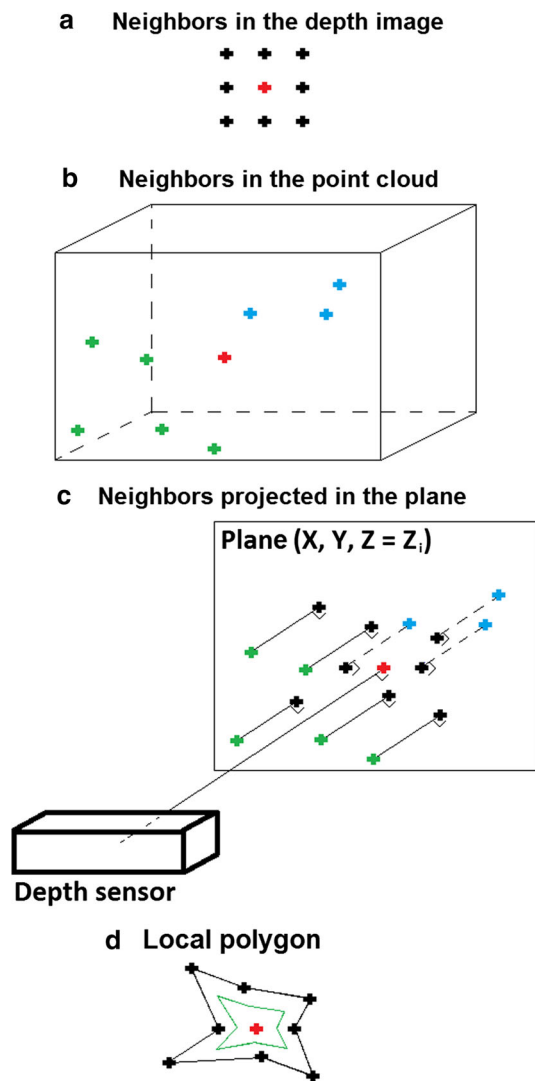


Fig. 3 Main steps used to compute the local effective volume. **a** A local depth image. The *red cross* is the current point i and *black crosses* are its neighbours. **b** The corresponding local point cloud. The *red cross* is the current point i with a depth value Z_i , *green crosses* are its neighbours with Z less than Z_i , *blue crosses* are its neighbours with Z more than Z_i . **c** Neighbours of the current point i are projected in the plane (X, Y, Z_i) . **d** Vertices of the local polygon are fixed at mid-distance between the current point and projections of its neighbours (*green line*)

polygon around a point. First, the local depth image is used to determine neighbours of the point i (see Fig. 3a). Then, in the local point cloud (see Fig. 3b), neighbours of the point i are projected onto the plane (X, Y, Z_i) (see Fig. 3c). To avoid redundancy, local polygon vertices are fixed at mid-distance between point i and the projections of its neighbours (see Fig. 3d). Knowing the local polygon vertices, the area of the local polygon can be computed and then the local effective volume. The global effective volume of the point cloud is the sum of all local effective volumes of the point cloud.

For methodological purposes, we test our algorithm of effective volume on a calibrated object composed of differ-

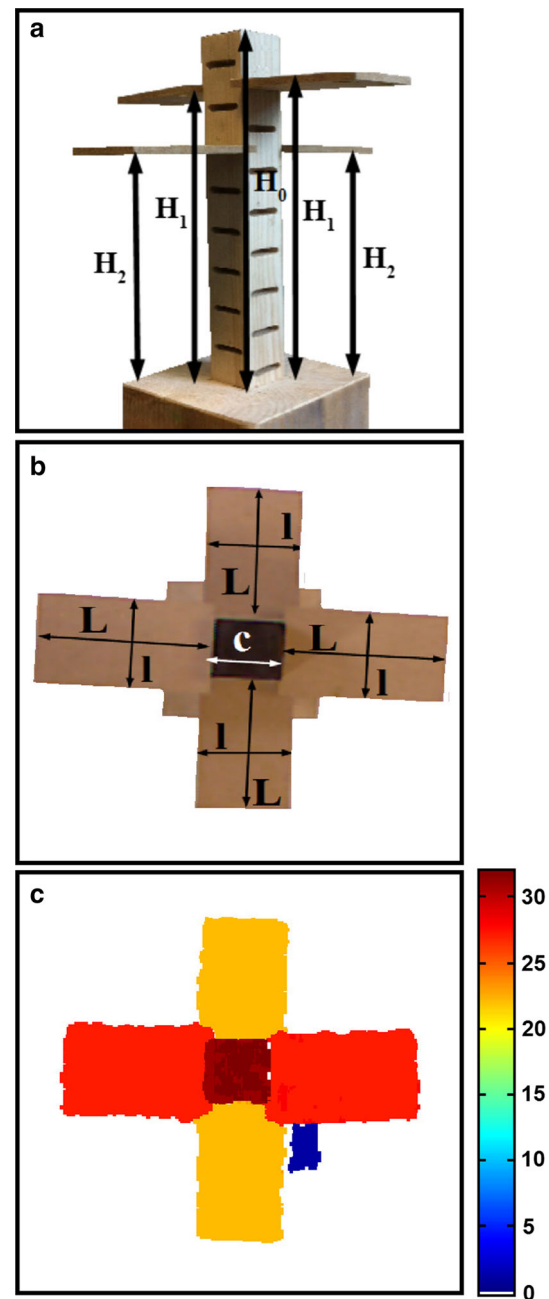


Fig. 4 The calibration object with a known effective volume. **a** RGB image of a lateral view ($H_0 = 31$ cm, $H_1 = 27$ cm and $H_2 = 21.5$ cm). **b** RGB image from a top view ($L = 10$ cm, $l = 6$ cm et $c = 4$ cm). **c** Depth image from a top view. *Colorbar* values gives the difference between the maximum depth and the local depth (values are in cm). The theoretical effective volume is $H_0 \times c \times c + 2 \times L \times l \times (H_1 + H_2) - 4 \times H_2 \times l \times l = 6230$ cm³. The theoretical real volume is $4 \times L \times l \times e + c \times c \times H_0 = 640$ cm³ with $e = 0.6$ cm, the thickness of all planes. The convex hull volume, computed on the point cloud of the calibrated object [7], is 11,247 cm³

ent planes as visible in Fig. 4. To estimate its theoretical effective volume, we have considered a top view (90° from planes) and we have measured its dimensions with a millimetre precision ruler. Then, we applied the geometric formula

given in Fig. 4. We obtained an effective volume equal to 6230 cm^3 which is, given the uncertainty of both methods (manual and computed), in agreement with the effective volume 6847 cm^3 computed from the depth image of Fig. 4c. For this calibrated object, the effective volume is larger than the real volume but smaller than the convex hull volume (see Fig. 4).

3.2 Multiscale analysis

In recent publications, [25–27] performed multiscale analyses on the colour images from natural scenes. Reference [15] extended these studies to depth images from natural wood scenes. Multiscale analysis can be done using several statistical tools. In this article, we propose to apply the number of neighbours method [25] and the box counting method [27] for depth characterization of the shoots of plants through 3D spatial scales.

In a point cloud, for each point i , the number of neighbours $N_i(r)$ lying within a spherical neighbourhood with radius r is calculated. For each radius r , the average $N(r)$ of the $N_i(r)$ is computed over all points i of the point cloud serving as a centre of sphere of radius r . Only spheres that are completely in the point cloud limits are considered [25].

We also compute another multiscale analysis tool, the box counting. In a point cloud, the box counting $NB(r)$ is found in terms of r with r the side length of given boxes. For each side length, $NB(r)$ is the number of boxes with side length r which are needed to cover all the point cloud [27].

For methodological purposes, we propose to perform the multiscale analyses of a uniformly distributed random 3D point cloud shown in Fig. 5a. Its multiscale analysis by the number of neighbours method is given in Fig. 5b, where a power law with a slope of +3 in a log–log scale is found as predicted by theory: since the points are uniformly distributed in 3D, the average number $N(r)$ of neighbours in a sphere of radius r grows as the volume $\sim r^3$ of the sphere. The multiscale analysis by the box counting method is given in Fig. 5c, where a power law with a slope of –3 in a log–log scale is found as predicted by theory: since the points are uniformly distributed in 3D, the average number $NB(r)$ of boxes of side r needed to cover the point cloud decreases as the volume r^3 of each box increases.

3.3 3D symmetry

To quantify 3D symmetry, we define three planes along each of the three axes (X, Y, Z) of the point cloud (see Fig. 6). These three planes can be used to compute three different symmetries : longitudinal, transversal and parallel. For each of these symmetries, we count the number of points with a symmetric matching. To remain insensitive to the observation

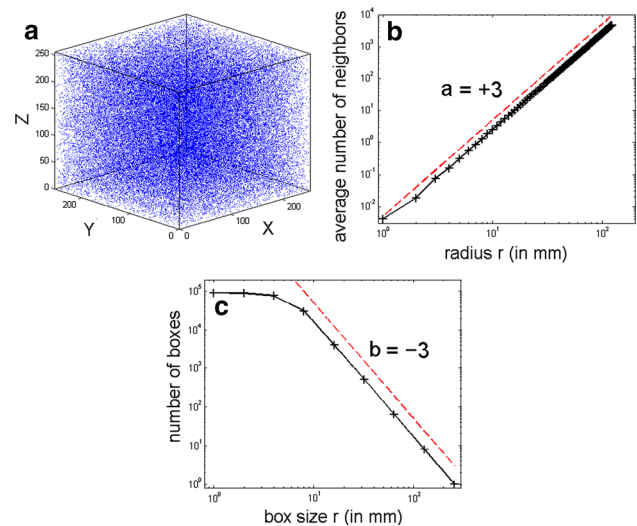


Fig. 5 Multiscale analyses of a uniformly distributed random point cloud . **a** The 3D point cloud . **b** The corresponding average number of neighbours $N(r)$ following a power law with a slope of +3 in a log–log scale. **c** The corresponding average number of covering boxes $NB(r)$ following a power law with a slope of –3 in a log–log scale. In **b** and **c** the dashed line materializes respectively the slope +3 and –3.

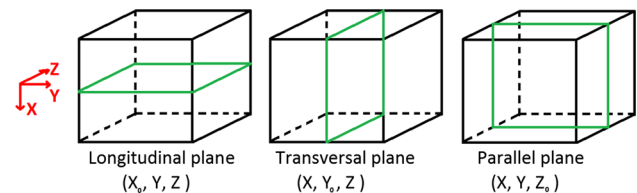


Fig. 6 Three planes defined in three different space directions. The plane (X_0, Y, Z) , with X_0 a constant, defines the longitudinal plane, the plane (X, Y_0, Z) , with Y_0 a constant, defines the transversal plane and the plane (X, Y, Z_0) , with Z_0 a constant, defines the parallel plane

scale of the plant, we always use a ratio between this number of points and the total number of points in the current point cloud. Finally, the 3D symmetry is defined by the mean of the three defined ratios of symmetry.

Computations of longitudinal and transversal symmetries are computed on the point cloud follow the same principle and can be done from only one point cloud provided by a depth sensor. In this part of the article, we focus the explanations on the algorithm of longitudinal symmetry, the symmetry in terms of the plane (X_0, Y, Z) (see Fig. 6). For a given point cloud, we fix X_0 as the middle value between minimum and maximum values of the X coordinate. In this point cloud, a point (X_i, Y_i, Z_i) with $X_i < X_0$ has a symmetric matching if there exists a point (X_j, Y_j, Z_j) with $X_j = -X_i$ (relative to X_0), $Y_j = Y_i$ and $Z_j = Z_i$. The value range of the longitudinal symmetry ratio is $\{0 \dots 0.5\}$. For methodological purposes, we propose to check the computation of longitudinal symmetry on the synthetic point cloud associated with the depth image of Fig. 7. Its theoretic-

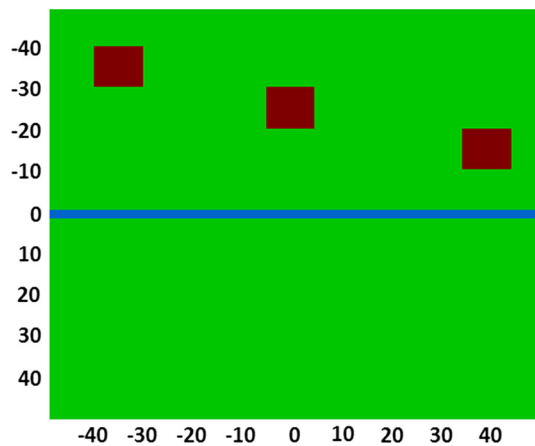


Fig. 7 The depth image of a synthetic point cloud with a known longitudinal symmetry. *Left values* indicate the evolution of X coordinates in the point cloud and *bottom values* the evolution of Y coordinates. *Red* and *green* pixels have different depth values and blue pixels have a zero value. The size of the depth image is 100×100 pixels. Due to pixels with a zero value (2 lines around X_0 to show the symmetry axis), the associated point cloud contains 9800 points. X_0 is equal to zero. Three squares of size 10×10 pixels have nonsymmetric matching. So, there are $4900 - 3 \times 10 \times 10 = 4600$ pixels belonging to the *top* part of the point cloud ($X < X_0$) with a symmetric matching in the *bottom* part. So, the longitudinal symmetry ratio of this synthetic point cloud is $\frac{4600}{9800} = 0.47$

cal longitudinal symmetry ratio is known and equal to 0.47. The application of the longitudinal symmetry algorithm on this point cloud gives a result in accordance with theoretical expectations.

In a point cloud provided by the depth sensor, two points cannot have the same X and Y coordinates. So, the computation of the parallel symmetry, the symmetry in terms of the plane (X, Y, Z_0) (see Fig. 6), cannot be done, like previously, with only one point cloud. To solve this constraint, we compute the parallel symmetry from two point clouds of the shoots of plants: the point cloud of the current view (view 1 in Fig. 8a) and the point cloud of the view acquired after a rotation of 180° (from the current position) by the motorized depth sensor (view 2 in Fig. 8a). In this case, the number of symmetric matchings for the parallel symmetry is the number of points with the same coordinates (X, Y, Z) in the two point clouds. The value range of the parallel symmetry ratio is $\{0 \dots 1\}$. For methodological purposes, we set a synthetic point cloud (associated with the depth image of Fig. 8b), corresponding to view 1 in Fig. 8a, and also a synthetic opposite point cloud (associated to the depth image of Fig. 8c), corresponding to view 2 in Fig. 8a. The parallel symmetry ratio between these two synthetic point clouds is known and equal to 0.89. The computation of the parallel symmetry algorithm on these point clouds gives a parallel symmetry ratio equal to the theoretical prediction.

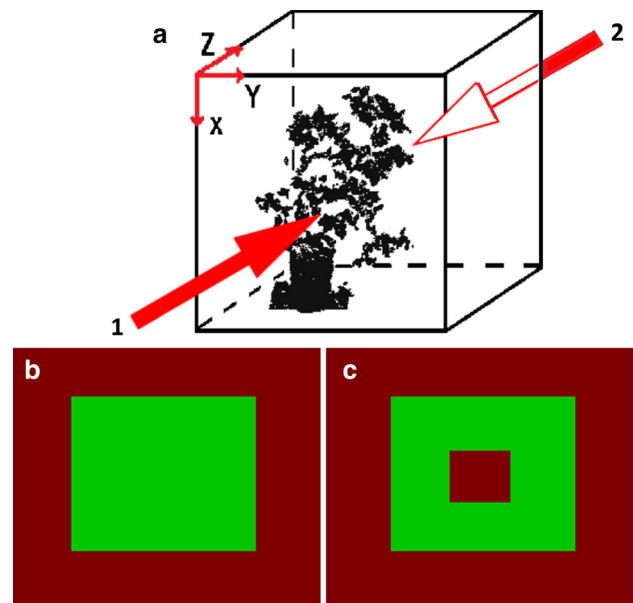


Fig. 8 Two different point clouds are used to compute the parallel symmetry. **a** The parallel symmetry is computed from two point clouds: the current point cloud (view 1 in this picture) and the opposite point cloud acquired after a rotation of 180° of the motorized depth sensor (view 2 in this picture). **b** The depth image of a synthetic point cloud. *Green* pixels correspond to nonzero depth while *red* pixels to zero depth. The size of the depth image is 100×100 pixels and the size of the nonzero depth square is 60×60 pixels (3600 points in the point cloud). **c** The depth image of the corresponding opposite point cloud. It is the clone of the previous depth image except that there is a square of size 20×20 pixels (400 points in the point cloud) with depth equal to zero inside the square of nonzero depth. So, the expected parallel symmetry ratio is $\frac{3600-400}{3600} = 0.89$

To illustrate the 3D symmetry, we compute it on the point cloud of the three objects of Fig. 9. The first one is a sphere (see Fig. 9a), an object perfectly symmetric in terms of each symmetry plane of this study. So, its longitudinal and transversal ratios are 0.5 and its parallel ratio is 1. The second one is a pyramid with a square base, an object perfectly symmetric in terms of transversal and parallel planes but totally asymmetric in the longitudinal direction. Thus, its transversal ratio is 0.5, its parallel ratio is 1 and its longitudinal ratio is 0. The last one is a well-known Venus head whose point cloud can be found in [28]. This object is not totally symmetric or asymmetric in each direction, so its longitudinal ratio is 0.3, its transversal ratio is 0.2 and its parallel ratio is 0.1.

In this study, we use three particular planes but the symmetry can be computed from an infinite number of others planes. In addition, principal component analysis approaches (encompassing ellipsoid, fractional anisotropy, ...) could be used to extract a global information of the point cloud symmetry. All these symmetry methods are complementary to the proposed 3D symmetry and they could be useful for the depth characterization of the shoots.

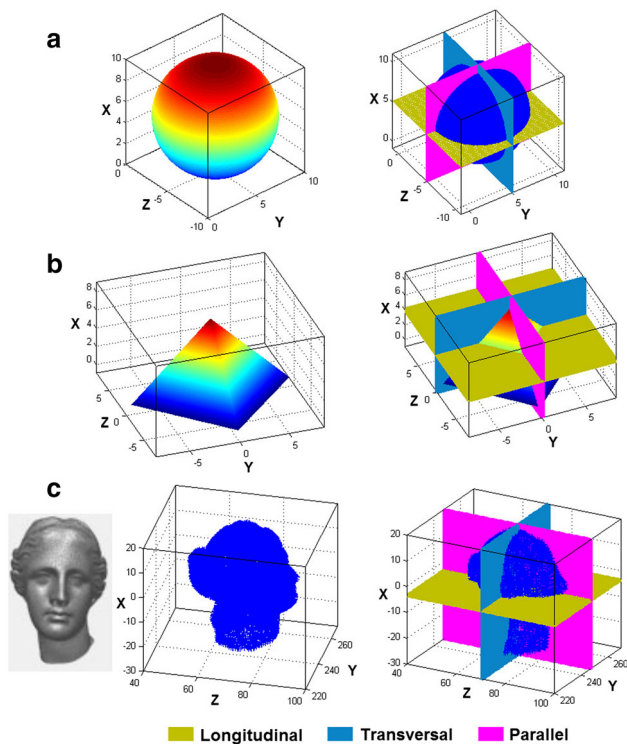


Fig. 9 Three different objects with three different 3D symmetries: **a** Sphere with longitudinal ratio = 0.5, transversal ratio = 0.5 and parallel ratio = 1. **b** Pyramid with longitudinal ratio = 0, transversal ratio = 0.5 and parallel ratio = 1. **c** Venus head with longitudinal ratio = 0.3, transversal ratio = 0.2 and parallel ratio = 0.1 (the right image is extract from [28])

3.4 Hole ratios

Multiple reflections of light in the shoots, diffusions, absorptions and shading result in the creation of zones of non-defined depth (depth set to zero) in the depth image. These zones can be considered as lacunarity holes and indicate that light has been trapped in the plant. In addition, light may also pass through the shoots resulting in transmission holes in the depth image (nonzero pixels not belonging to the plant). We propose to use lacunarity and transmission surfaces for the depth characterization of the shoots of plants.

Practically, to find lacunarity and transmission surfaces, the depth image must be acquired in a closed room, whose dimensions belong to the depth interval accessible with the depth sensor. In these conditions, as shown in Fig. 10, depth images were always composed of three distinct populations: the plant, the background and the non-defined zones. With such high contrast, the well-known automatic thresholding method of Otsu [29] efficiently segments the plant in the depth images. Then, to remain insensitive to the observation scale of the plant, we always use a ratio between the surface area (lacunarity or transmission) and the total surface of the plant. Only surfaces in the convex hull of the plant are taken into account.

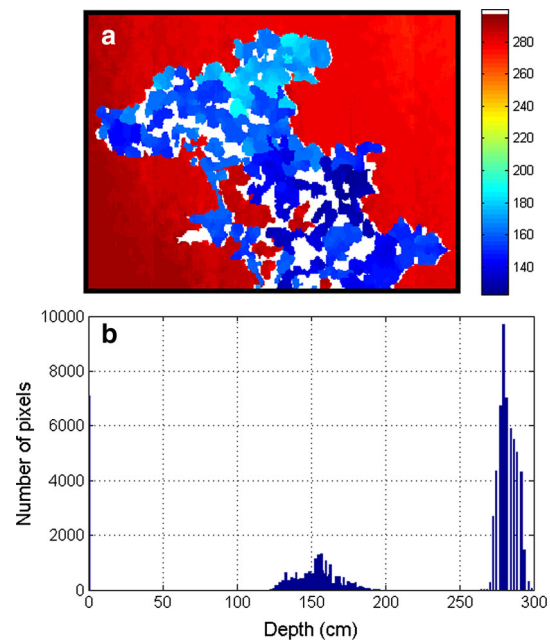


Fig. 10 An example of depth image composed of three different populations: the plant (depth around 150 cm), the background (depth around 280 cm) and the non-defined zones (depth equal to zero). **a** The depth image. **b** The corresponding histogram of depth

For methodological purposes, we illustrate the computation of the hole ratios on a synthetic depth image. Figure 11 shows this depth image (a) and different binary images (b, c, d) used to find hole surfaces. Background and lacunarity holes are studied into the convex hull of the plant (see Fig. 11b). Background holes correspond to pixels with a background value in this convex hull (see Fig. 11c), while lacunarity holes are pixels with a zero value (see Fig. 11d). The computation of our algorithm on this synthetic depth image gives hole ratios equal to the theoretical prediction : 0.54 for the transmission ratio and 0.17 for the lacunarity ratio.

4 Application to plants

We are now ready to use the motorized depth sensor of Sect. 1 to compute the four new shape descriptors of the previous section all around real plants. We acquired with the motorized depth sensor 72 depth images all around two real plants shown in Fig. 12. The plant *A* is a rosebush (*Rosa hybrida*) and the plant *B* is a snake plant (*Sansevieria trifasciata*). These plants are specially chosen to present very different shoots. The shoots of plant *A* occupy a larger range of space than plant *B* and it is composed of leaves (assembling of small leaflets) with different orientations. By contrast to plant *A*, the shoots of plant *B* are composed of large, flat and regular leaves. In the sequel, we compare the application of our four

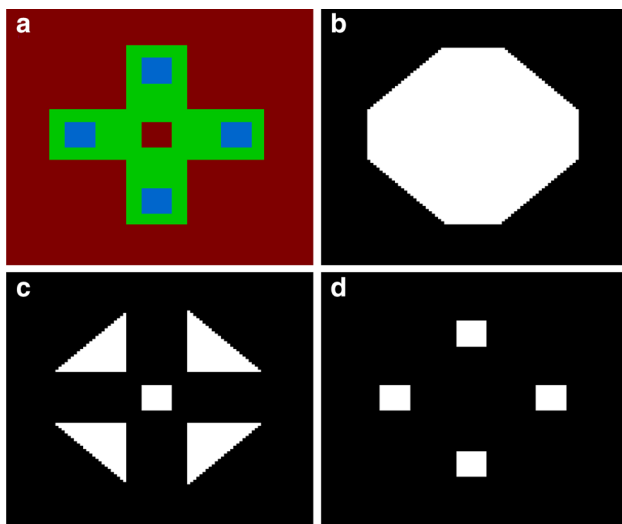


Fig. 11 The hole ratio computation based on three binary images obtained from the depth image. **a** A synthetic depth image. *Green* pixels correspond to plant, *red* pixels to background and *blue* pixels to lacunarity. **b** The corresponding binary image of the convex hull. **c** The corresponding binary image of background holes in the convex hull. **d** The corresponding binary image of lacunarity holes in the convex hull. The plant is composed of two *rectangles* of size 80×20 pixels which cover themselves on 20×20 pixels. There are four transmission *triangles* (*rectangle* and *isoscele*) with side length equals to 24 pixels and a transmission *square* of size 10×10 pixels. There are four lacunarity *squares* of size 10×10 pixels. The transmission ratio is $\frac{10 \times 10 + 4 \times \frac{24 \times 24}{2}}{2 \times 80 \times 20 - 20 \times 20 - 5 \times 10 \times 10} = 0.54$ and the lacunarity ratio is $\frac{4 \times 10 \times 10}{2 \times 80 \times 20 - 20 \times 20 - 5 \times 10 \times 10} = 0.17$

new shape descriptors on the 72 depth images acquired all around these two different plants.

4.1 Effective volume

The computation of the effective volume on the point cloud of the shoots of plants gives access to the metric volume, in m^3 , of its visible part from the depth sensor point of view. In this study, the shoots of plant *A* occupy a larger range of space than plant *B*, but the depth images of these two plants have been acquired with two different observation scales. Following these setting up changes, the shoots of plants *A* and *B* have roughly the same number of pixels (i.e. the same apparent surface) in the depth images of the Fig. 13a, b. So, from these images, the two plants cannot be distinguished from the computation of their apparent surface. However, the shoots of plant *A* show a larger range of depth than plant *B* (70 cm for plant *A* versus 30 cm for plant *B*). This difference in the range of depth results in a larger computed effective volume for the shoots of plant *A*. Thus, beyond the apparent surface, the effective volume computed from the shoot point clouds allows obtaining a relative difference between plants *A* and *B* in terms of space filled by the shoots.

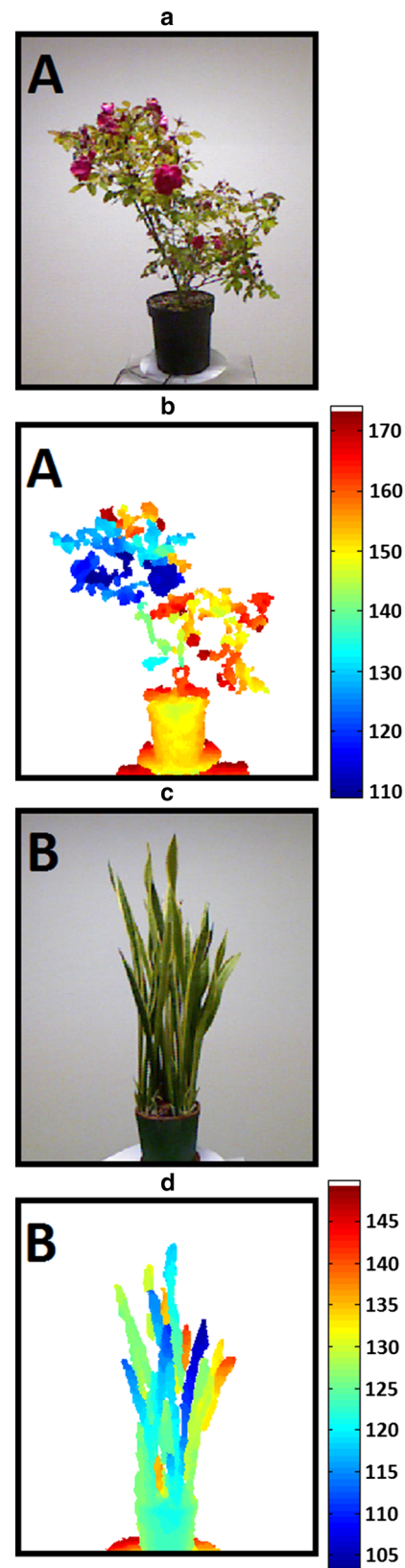


Fig. 12 **a, c** RGB view of the plants *A* and *B*. **b, d** Corresponding depth images (depth values are in cm)

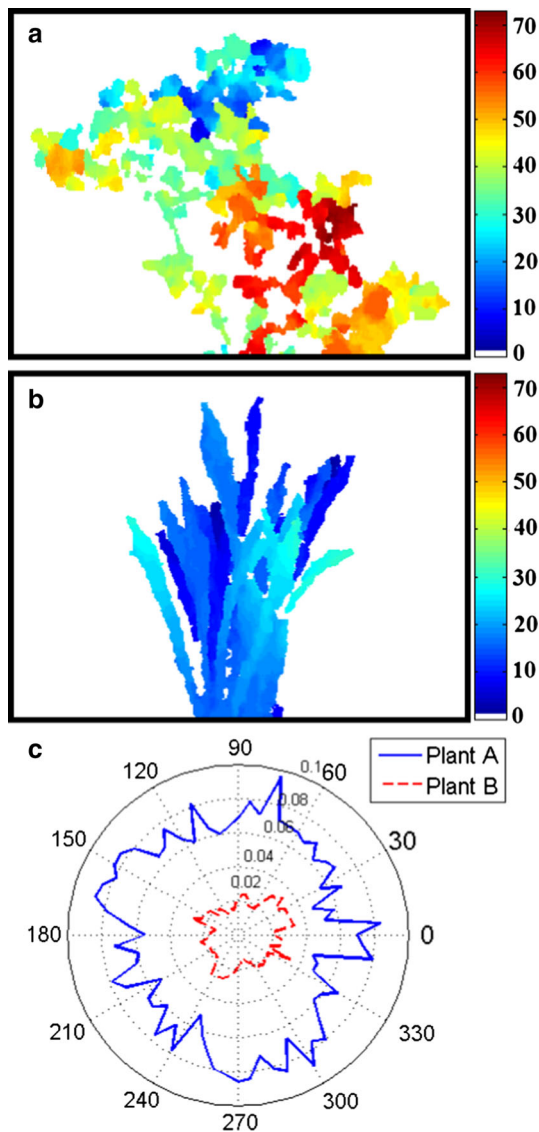


Fig. 13 The computation of the effective volume all around real plants. **a, b** Depth images of the shoots of plants A and B from Fig. 12 at an observation angle of 75°. *Colorbar* values give the difference between the maximum depth and local depth values (values are in cm). **c** Polar plot of the effective volume in m³ as a function of the angle of observation. *Solid line* is for plant A, *dotted line* for plant B

In this study, for all the point clouds at all angles of view acquired with the motorized depth sensor, the range of depth of plant A is always larger than that of plant B. So, as shown by Fig. 13c, the effective volume of the shoots of plant A computed all around the rotation stays larger than that of plant B. For both plants in the used setting up, this effective volume is relatively constant all around the plant. For other settings or other plants, larger variations may occur in the range of depth around the plant according to the angle of view. A single evaluation of the effective volume, from a single angle of view, could, therefore, lead to misinterpretation of the actual 3D space filled by the plant. By contrast, the computation of

the effective volume from data acquired from multiple angles of view with the motorized depth sensor allows to accurately describe the space filled by the shoots.

4.2 Multiscale analysis

The multiscale analysis of the point cloud of the shoots of plants is realized by means of the number of neighbours method and of the box counting method. We especially want to test for the average number of neighbours $N(r)$ and for the average number of covering boxes $NB(r)$, the possibility of power laws of the forms $N(r) \sim r^a$ and $NB(r) \sim r^{-b}$. The presence of such power-law evolutions identifies regularity or self-similarity across scales for the spatial organization of the point cloud. They can be interpreted in relation to the following references [25–27]: When the points in the cloud distribute in a volume with three-dimensional organization, then one has the evolutions $N(r) \sim r^3$ and $NB(r) \sim r^{-3}$, as in the example of Fig. 5. When the points distribute in a surface-like organization with two dimensions, one has $N(r) \sim r^2$ and $NB(r) \sim r^{-2}$. When the points distribute with a curvilinear organization with one dimension, one has $N(r) \sim r^1$ and $NB(r) \sim r^{-1}$. Power laws of the form $N(r) \sim r^a$ and $NB(r) \sim r^{-b}$ with noninteger exponents a and b , identify fractal organizations that interpolate between these regular shapes.

Figure 14a, b gives the average number of neighbours $N(r)$ computed on one point cloud, respectively, for plants A and B from Fig. 12. Both numbers of neighbours evolutions follow power laws $N(r) \sim r^a$ with exponent $a \neq 0$. Slopes in

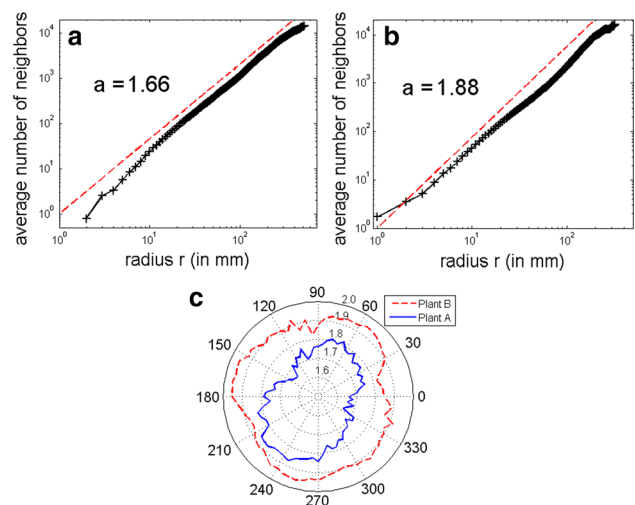


Fig. 14 Multiscale analysis by the number of neighbours method. **a, b** Number of neighbours $N(r)$ of plants A and B from Fig. 12 at the observation angle of 355°. The *dashed line* materializes the slope of the followed power law in the log–log scale. **c** Polar plot of the exponent a of the power law followed by the number of neighbours $N(r)$ as a function of the angle of observation. *Solid line* is for plant A, *dotted line* for plant B

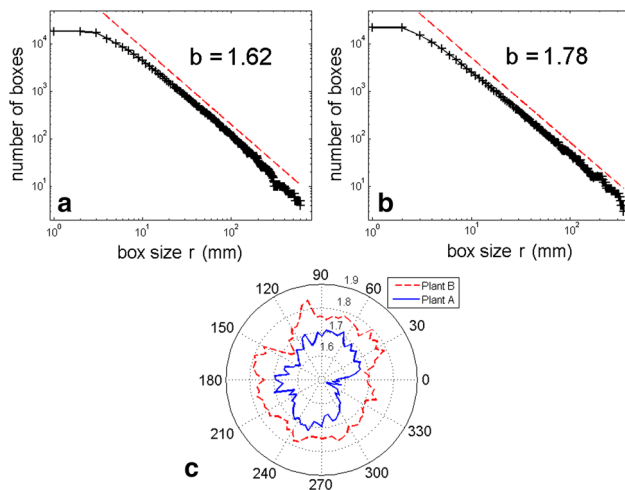


Fig. 15 Multiscale analysis by the box counting method. **a, b** Number of neighbours evolutions of plants *A* and *B* from Fig. 12 at the observation angle of 150° . The *dashed line* materializes the slope of the followed power law in the log–log scale. **c** Polar plot of the exponent b of the power law followed by the box counting $NB(r)$ as a function of the angle of observation. *Solid line* is for plant *A*, *dotted line* for plant *B*

a log–log scale of these power laws are different ($a = +1.66$ for plant *A* and $a = +1.88$ for plant *B*). As shown in Fig. 15a, b, the box counting evolutions for the same two plants follow power laws $NB(r) \sim r^{-b}$ with exponent $b \neq 0$ over a large range of box sizes. Like number of neighbour evolutions, slopes in a log–log scale of these power laws are different ($b = 1.62$ for plant *A* and $b = 1.78$ for plant *B*). Exponents a and b of power laws followed during multiscale analyses depend on the complexity of the shoots of the observed plant. For all point clouds around a plant, multiscale analyses follow power laws. So, we use evolutions of exponents a and b during the rotation of the motorized depth sensor to characterize the depth of the shoots all around the plant. Figures 14c, and 15c, respectively, give evolutions of exponents a and b obtained by computing the number of neighbours and box counting on point clouds all around plants *A* and *B*. Shoots of these two plants keep their structure unchanged for all rotation steps of the motorized depth sensor. So, exponents a and b of multiscale analyses stay globally constant during the rotation. The multiscale analysis (number of neighbours and box counting) characterizes the complexity of the shoots of the observed plant. Its computation all around the plant characterizes changes in this complexity. Moreover, regular power laws with non-integers exponents a and b , as consistently observed for the plants tested here, suggest a fractal organization of the shoots of plants, exhibiting self-similarity across scales in their spatial structure.

The non-integer exponents a and b observed between 1 and 2 identify the plant foliage as irregular fractal shapes with a space-filling geometry which is less dense than a uniform surface, but more dense than a regular line. At a

qualitative level, this global structural property is consistently observed for the two plants *A* and *B* here; yet at a finer quantitative level, differences are measured in the specific values of the fractal exponents a and b providing a differential characterization of the foliage of the two plants *A* and *B*. Larger exponents a, b closer to 2 are consistent for plant *B* with relatively flat and more regular leaves coming closer to a flat surface. Meanwhile, smaller exponents a, b are consistent for plant *A* with higher lacunarity and irregular leaves further away from a flat surface. Fractal organizations have been reported for plants from various quantitative measurements [30]. They are confirmed here from the new measurement derived from depth images as presented here.

4.3 3D symmetry

The 3D symmetry of the shoots of plants is computed from three different symmetries: longitudinal, transversal and parallel. Generally, the shoots have a non regular architecture and the probability to have any exact symmetric matchings is very low. So ratios of symmetry with depth in millimetre, as provided by the depth sensor, would be close to zero. In this study, to compare the symmetry of plants, plant 3D coordinates (X, Y, Z) are rounded in decimetre. Figure 16 gives

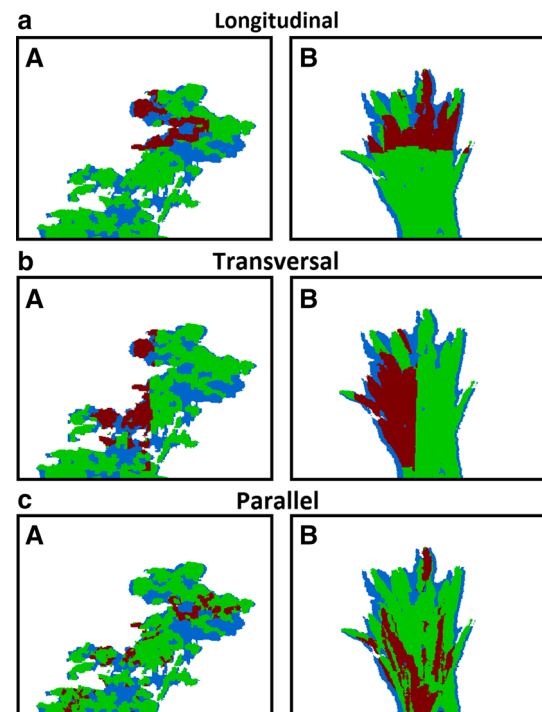


Fig. 16 Illustrations of the computation of 3D symmetry on the point clouds of plants *A* and *B* from Fig. 12. **a** Longitudinal symmetry. **b** Transversal symmetry. **c** Parallel symmetry. The observation angle is 210° . *Red* pixels correspond to points with a symmetric matching, *green* pixels to points of plant without symmetric matching and *blue* pixels to lacunarity pixels

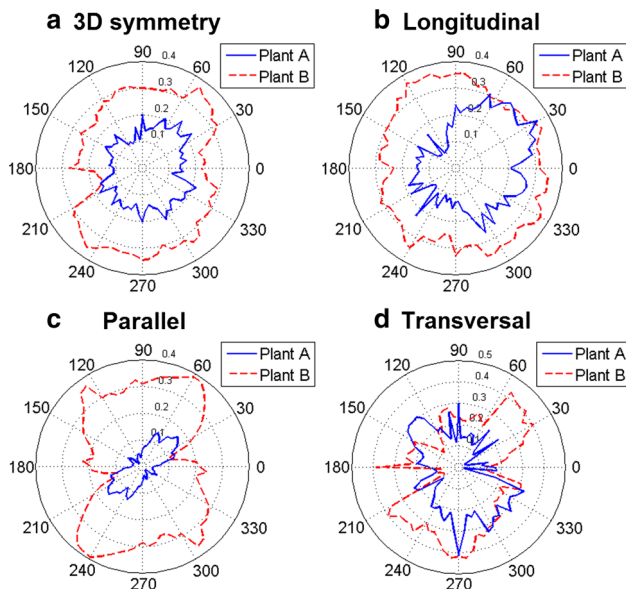


Fig. 17 The computation of the 3D symmetry all around real plants. **a–d** Polar plot of the considered symmetry as a function of the angle of observation. *Solid line* is for plant *A* and *dotted line* for plant *B*

illustrations of longitudinal, transversal and parallel symmetry computations on point clouds of plants *A* and *B* from Fig. 12. In these illustrations, for all types of computed symmetry, plant *B* has more symmetric matchings and relatively the same number of points in the point cloud than plant *A*, resulting in a larger computed 3D symmetry for plant *B* (mean of the longitudinal, transversal and parallel symmetries). This result is in accordance with both shapes of studied plants. Indeed, the large and vertical leaves positioned following a circle of plant *B* give a shape globally symmetric, while the complex structure with different axes of plant *A* results in a less symmetric shape.

As shown in Fig. 17a, the computed 3D symmetry evolves with the rotation of the motorized depth sensor thus expressing the anisotropy of the global symmetry of the shoots of plants. The computed 3D symmetry around both plants is not constant but it globally follows the expected evolutions: 3D symmetry of plant *B* stays larger than plant *A*. So, the proposed 3D symmetry coupled with the motorized depth sensor provides a good descriptor of the real shape of the plant, allowing to describe the symmetry anisotropy of the shoots. The same behaviour is globally obtained for longitudinal and parallel symmetries (see Fig. 17b, c). However, the transversal symmetry of both plants is different and some observation angles give plant *A* a more symmetrical appearance than plant *B*. It is in accordance with the shape of plant *B* because this plant has few leaves tilted on side which shift the centre of symmetry and decrease the value of transversal symmetry. So, while the 3D symmetry provides a global information of symmetry, each individual symmetry (longitudinal, transver-

sal or parallel) gives a finer information about the shape of the plant because it is focused in only one direction of space.

4.4 Hole ratios

The transmission and lacunarity ratios are, respectively, based on the surface of background and lacunarity holes inside the convex hull of the shoots of the observed plant. Figure 18a, b gives illustrations of the hole ratios computations on depth images, respectively, for plants *A* and *B* of Fig. 12. In these illustrations, the computed hole ratios are smaller for plant *A* than for plant *B*. In a depth image, the computed transmission ratio quantifies the proportion of leafless zones in the shoots (red pixels in Fig. 18a, b). Since the

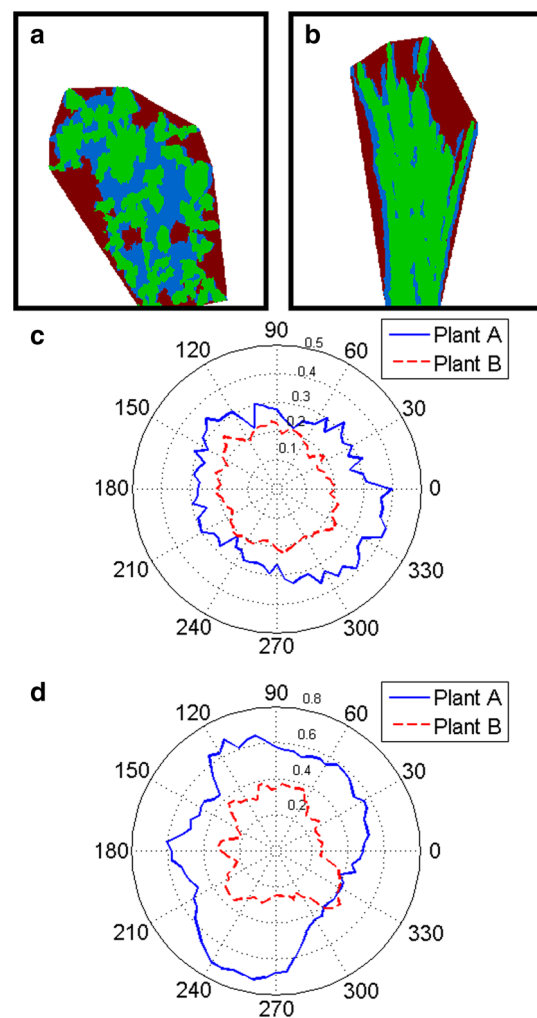


Fig. 18 The computation of the hole ratios all around real plants. **a, b** Illustrations of computations of the hole ratios on depth images at the observation angle of 355° for plants *A* and *B* from Fig. 12. *Red* pixels correspond to background, *green* pixels to plant and *blue* pixels to lacunarity. **c, d** Polar plot of the lacunarity and transmission ratios as a function of the angle of observation. *Solid line* is for plant *A*, *dotted line* for plant *B*

shoots of plant *A* are less concentrated and more scattered than those of plant *B*, its depth image has a larger proportion of background in its convex hull, around and in the shoots. This results in a computed transmission ratio larger for plant *A* than for plant *B*. So, the transmission ratio quantifies the shape of the shoots such as the higher transmission ratio, the higher the shape complexity of the plant. The computed lacunarity ratio estimates the proportion of zones where the sensor is unable to return a depth measurement because of shading and constitution of the shoots (blue pixels in Fig. 18a, b). Since the shape of plant *A* is less regular, shading is accentuated. In addition, contrary to vertical and large leaves of plant *B*, the small leaves with different orientations of plant *A* lead to a high probability of light trapping. Consequently, the computed lacunarity ratio is larger for plant *A* than for plant *B*. Summarizing, the lacunarity ratio estimates the global constitution, association of the number, the size, the shape, the orientation and the spatial organisation of leaves, of the shoots such as the higher lacunarity ratio, the higher the constitution complexity of the plant.

As shown by Fig. 18c, d, the hole ratios computed on the depth images of the motorized depth sensor stay globally larger for plant *A* than for plant *B*. This result is in accordance with the global complexities of shape and constitution of both plants. However, for few angles of view, values of plant *B* are equal or larger than that of plant *A*. So, to accurately describe the global complexity (shape or constitution) of shoots of plants, hole ratios must be computed on different angles of view as proposed in this study.

For a complementary appreciation of the behaviours and capabilities of the new descriptors, we have also applied the approach systematically on a set of nine more plants, chosen to cover a wider range of possible shapes, as presented in Fig. 19. The computation of the four proposed shape descriptors has been carried out, and the complete results for the nine plants of Fig. 19 are made accessible in [34]. For illustration, we show in Fig. 20, one among those descriptors, the transmission ratio of the shoots, computed for the nine plants of Fig. 19, and displayed as a function of the angle of rotation around each plant. As defined in Sect. 4.4, the transmission ratio quantifies the proportion of leafless or open zones in the convex hull of the shoots. On the illustration of Fig. 20, it is notable that the isotropic aspect of transmission ratio and the average value of the transmission ratio display capabilities for discrimination between plants. Considering two plants of different species (for instance Plant1 and Plant2 in Fig. 19), having different shape, size and spatial organization of leaves and shoots, the average ratio differs by a factor of 2 between them. Average transmission ratio is of 0.25 for Plant1 and of 0.5 for Plant2. This is in good agreement with a visual appreciation as Plant1 has big leaves with different orientations with a high probability of light interception leading to a smaller transmission ratio than Plant2, which owns

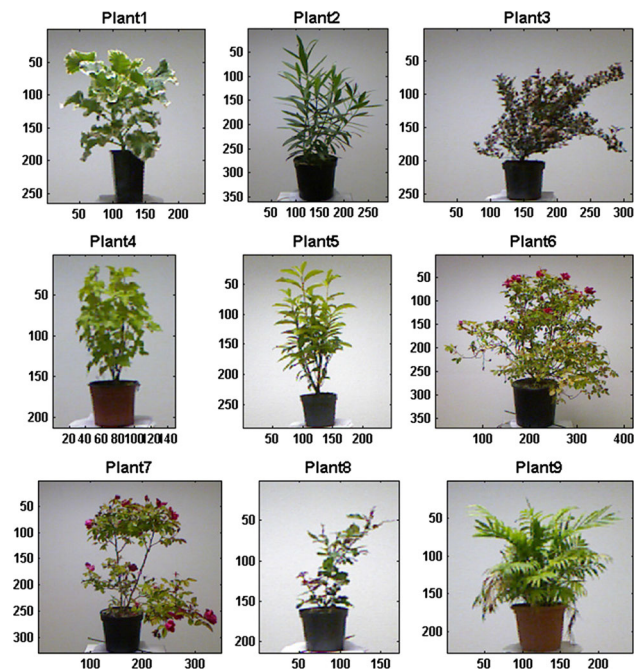


Fig. 19 Panel of RGB views of nine other plants

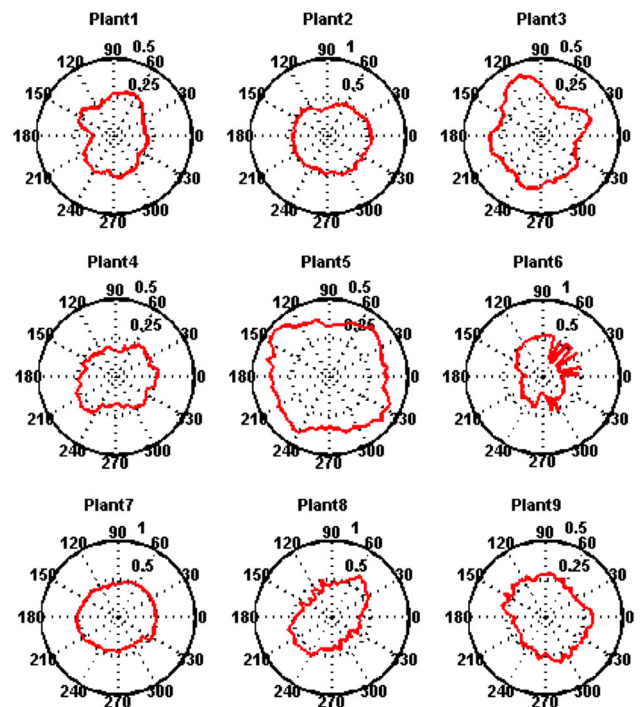


Fig. 20 Polar plot of the transmission ratio as a function of the angle of observation computed for the nine plants of Fig. 19

smaller leaves with orientation in extension of shoots. Considering two plants of the same species (for instance rosebush as Plant6 and Plant7 in Fig. 19), having different spatial organization of shoots, the average transmission ratio is of 0.5 for both but the isotropic aspect is clearly not equal according to

angle of observation. This is again in a relatively good agreement with a visual appreciation of both plants as Plant6 is bushy according to some specific direction, whereas Plant7 is relatively sparse in its central part.

Further analysis could be developed by confronting the whole set of descriptors given in [34], especially to question what would be the best descriptors and the tolerated error. The answer would depend on the plant science question raised. For instance, in the study [19] on rosebushes, we demonstrated that all the ten incorporated botanistic descriptors were important to discriminate the ornamental value of the different phenotypes of plants tested. For breeders, who are seeking the highest production, the descriptors attached to the volume would take a greater importance with a higher sensitivity on errors. Also more systematic studies could be undertaken on more instances and plants, especially for an appreciation of the robustness and sensitivity of the proposed descriptors in relation to the variability in the plants involved in the analysis. Such extensive studies, however, lie beyond the scope of the present paper, which concentrates on the definition of a new methodology for plant shape characterization from depth data with some illustrations.

5 Conclusion

Depth data are becoming more and more widely accessible by means of new low-cost sensors as reported in the paper. We have described here an integrated solution using a depth sensor coupled to a motorized turntable devised for a quantitative characterization of the spatial 3D structure of plants. We have introduced four new shape descriptors to characterize the shoot of an entire plant from multiple side views acquired from the depth camera: the effective volume (volume in m^3 seen by the depth sensor point of view) characterizes plants in terms of their size. Multiscale analysis tools (number of neighbours and the box counting methods) determine the complexity and possible fractality of the shoots of the observed plant. The 3D symmetry (longitudinal, transversal and parallel symmetries) quantifies the anisotropy of the shoots of plants. The hole ratio composed with the transmission ratio and the lacunarity ratio, respectively, capture the fragmented aspect of the shoot and the lacunarity of the shoots in its depth. We have systematically validated these shape descriptors on numerical ground truth and have then tested them on nine real plants contrasted in terms of size, scales, symmetry and lacunarity. To this purpose, we have specially coupled the low-cost depth sensor of the Microsoft Kinect with a low-cost turntable. With such a multiple view depth sensor, a full 3D reconstruction of the shoot of the plant is possible for simple shoot as recently demonstrated [31–33]. However, for more complex shoots, like the ones tested in the report, a full 3D reconstruction from multiple

side views with depth cameras is expected to be a difficult task and only an appreciation of the overall shape of the plant is accessible. This is now possible quantitatively in depth with the shape descriptors introduced in this work.

We believe the evolutions of these shape descriptors all around the plants can be exploited to quantitatively characterize and discriminate a large number of plants. To go further, although the scope of study is more the definition of a new methodology for plant shape characterization from depth data, we have extended the application of our shape descriptors to nine other plants. These nine plants have been chosen to cover a wide range of shapes that may describe, in some extent, the variability of plants in terms of their varieties, ages or visual aspect. The computation of the four proposed shape descriptors has been done and results are accessible online [34]. Considering a reproducible science approach, the dataset of the associated depth images is also downloadable [34]. With such dataset, further studies could focus on classification problems to better appreciate robustness and sensitivity of the proposed descriptors. New shape descriptors could also be introduced and validated on this dataset.

Also, the depth characterization could be interestingly complemented with more classical descriptors based on colour or grey level images. This is easily feasible again with the Microsoft Kinect since the depth sensor is associated with a spatially coregistered RGB camera. Therefore, acquisition coupled with a turntable to produce multiple side views and analysis of the anisotropy of the plant shoots in RGB and depth is another interesting perspective accessible with the motorized depth sensor presented here. The sensor used in this study could itself receive attention for improvement. In this study we used 72 images around the plants because our motorized depth sensor provides this number. With this resulting 5° step redundancies are often present between different successive images. The good-enough number of images, although depending on the shoot shape, is probably less than 72, and further investigation to define it quantitatively would be an interesting perspective.

A domain of specific interest for the characterization of the ensemble of shoots from depth imaging as proposed in this manuscript is for the aesthetic rating of ornamental plants. In this context, recent studies [19,35,36] have demonstrated the possibility to classify rosebushes from sensory profiles preference based on visual inspection. In these works, the description is qualitative, performed on RGB images of real [19,35] or virtual [36] rosebushes. This establishes the importance of subjective descriptors such as symmetry, compactness and shape, in the aesthetic assessment of ornamental rosebush. By contrast here, we used a depth camera and the 3D descriptors introduced in this manuscript include such traits and, therefore, naturally appear as good candidates for automatic quantitative and objective classification of orna-

mental rosebushes based on depth imaging. Confronting our automated 3D shape descriptors with a sensorial rating by human experts would correspond to a further investigation.

Acknowledgments Yann Chéné acknowledges support from Région Pays de la Loire, France, for the funding of his Ph.D.

References

- Fiorani, F., Rascher, U., Jahnke, S.: Imaging plants dynamics in heterogenic environments. *Curr. Opin. Biotechnol.* **23**, 227–235 (2012)
- Subramanian, R., Spalding, E.P., Ferrier, N.J.: A high throughput robot system for machine vision based plant phenotype studies. *Mach. Vis. Appl.* **24**, 619–636 (2013)
- Hiremath, S., Tolpekin, V.A., van der Heijden, G., Stein, A.: Segmentation of *Rumex obtusifolius* using Gaussian Markov random fields. *Mach. Vis. Appl.* **24**, 845–845 (2013)
- Zeng, G., Birchfield, S.T., Wells, C.E.: Rapid automated detection of roots in minirhizotron images. *Mach. Vis. Appl.* **21**, 309–317 (2013)
- van der Heijden, G., Song, Y., Horgan, G., Polder, G., Dieleman, A., Bink, M., Palloix, A., van Eeuwijk, F., Glasbey, C.: SPICY: towards automated phenotyping of large pepper plants in the greenhouse. *Funct. Plant Biol.* **39**, 870–877 (2012)
- Bellasio, C., Olejníčková, J., Tesař, R., Šebela, D., Nedbal, L.: Computer reconstruction of plant growth and chlorophyll fluorescence emission in three spatial dimensions. *Sensors* **12**, 1052–1071 (2012)
- Azzary, G., Goulden, M.L., Rusu, R.B.: Rapid characterization of vegetation structure with a Microsoft Kinect sensor. *Sensors* **13**, 2384–2398 (2013)
- Biskup, B., Scharr, H., Schurr, U., Rascher, U.: A stereo imaging system for measuring structural parameters of plant canopies. *Plant Cell Environ.* **10**, 1299–1308 (2007)
- Omasa, K., Hosoi, F., Konishi, A.: 3D lidar imaging for detecting and understanding plant responses and canopy structure. *J. Exp. Bot.* **158**, 881–898 (2007)
- Bucksch, A., Fleck, S.: Automated detection of branch dimensions in woody skeletons of fruit tree canopies. *Photogramm. Eng. Remote Sens.* **77**, 229–240 (2011)
- Klose, R., Penlington, J., Ruckelshausen, A.: Usability study of 3D time-of-flight cameras for automatic plant phenotyping. *Bornimer Agrartechnische Berichte* **69**, 93–105 (2009)
- Kraft, M., Saloma De Freitag, N., Munack, A.: Test of a 3D time of flight camera for shape measurements of plants. In: *CIGR Workshop on Image Analysis in Agriculture*, Budapest, Hungary, 26–27 Aug 2010 (2010)
- Chéné, Y., Rousseau, D., Lucidarme, P., Bertheloot, J., Caffier, V., Morel, P., Belin, E., Chapeau-Blondeau, F.: On the use of depth camera for 3D phenotyping of entire plants. *Comput. Electron. Agric.* **82**, 122–127 (2012)
- Chéné, Y., Belin, E., Chapeau-Blondeau, F., Boureau, T., Caffier, V., Rousseau, D.: Anatomic-functional bimodality imaging for plant phenotyping: An insight through depth imaging coupled to thermal imaging. Chap. 9, in Dutta Gupta, S., Ibaraki, Y., (eds.) *Plant Image Analysis: Fundamentals and Applications*. CRC Press, Boca Raton (2015)
- Chéné, Y., Belin, E., Rousseau, D., Chapeau-Blondeau, F.: Multi-scale analysis of depth images from natural scenes: scaling in the depth of the woods. *Chaos Solitons Fractals* **54**, 135–149 (2013)
- Golbach, F., Kootstra, G., Damjanovic, S., Otten, G., van de Zedde, R.: Validation of plant part measurements using a 3D reconstruction method suitable for high-throughput seedling phenotyping. *Mach. Vis. Appl.* 1–18 (2015)
- Nguyen, T.T., Slaughter, D.C., Max, N., Maloof, J.N., Sinha, N.: Structured light-based 3D reconstruction system for plants. *Sensors* **15**(8), 18587–18612 (2015)
- Sansoni, G., Trebeschi, M., Docchio, F.: State-of-the-art and applications of 3D imaging sensors in industry, cultural heritage, medicine, and criminal investigation. *Sensors* **9**, 568–601 (2009)
- Garbez, M., Chéné, Y., Belin, É., Sigogne, M., Labatte, J.L., Hunault, G., Rousseau, D., Galopin, G.: Predicting sensorial attribute scores of ornamental plants assessed in 3D through rotation on video by image analysis: a study on the morphology of virtual rose bushes. *Comput. Electron. Agric.* **121**, 331–346 (2016)
- Khoshelham, K., Elberink, S.O.: Accuracy and resolution of Kinect depth data for indoor mapping applications. *Sensors* **12**, 1437–1454 (2012)
- <http://labjack.com/u3>
- <http://qt.digia.com/>
- <http://www.openni.org/>
- Schnabel, R., Wahl, R., Klein, R.: Efficient RANSAC for point cloud shape detection. *Comput. Graph. Forum* **26**, 214–226 (2007). (Blackwell Publishing Ltd)
- Chauveau, J., Rousseau, D., Richard, P., Chapeau-Blondeau, F.: Fractal structure in the color distribution of natural images. *Chaos Solitons Fractals* **42**, 472–482 (2009)
- Chauveau, J., Rousseau, D., Richard, P., Chapeau-Blondeau, F.: Multifractal analysis of three-dimensional histogram from color images. *Chaos Solitons Fractals* **43**, 57–67 (2010)
- Chauveau, J., Rousseau, D., Chapeau-Blondeau, F.: Fractal capacity dimension of three-dimensional histogram from color images. *Multidimens. Syst. Signal Process.* **21**, 197–211 (2010)
- Venus head point cloud. <http://www.dirdim.com> (2014)
- Otsu, N.: A threshold selection method from gray-level histograms. *Automatica* **11**, 23–27 (1975)
- Da Silva, D., Boudon, F., Godin, C., Sinoquet, H.: Multiscale framework for modeling and analyzing light interception by trees. *Multiscale Model. Simul.* **7**, 910–933 (2008)
- Paulus, S., Dupuis, J., Mahlein, A.K., Kuhlmann, H.: Surface feature based classification of plant organs from 3D laserscanned point clouds for plant phenotyping. *BMC Bioinform.* **14**, 238–249 (2013)
- Paulus, S., Schumann, H., Kuhlmann, H., Léon, J.: High-precision laser scanning system for capturing 3D plant architecture and analysing growth of cereal plants. *Biosyst. Eng.* **121**, 1–11 (2014)
- Paulus, S., Dupuis, J., Riedel, S., Kuhlmann, H.: Automated analysis of barley organs using 3D laser scanning: an approach for high throughput phenotyping. *Sensors* **14**, 12670–12686 (2014)
- http://lisabiblio.univ-angers.fr/PHENOTIC/Shape_descriptors.zip
- Boumaza, R., Huché-Thélier, L., Demotes-Mainard, S., Coz, E.L., Leduc, N., Pelleschi-Travier, S., Qannari, E.M., Sakr, S., Santagostini, P., Symoneaux, R., Gurin, V.: Sensory profiles and preference analysis in ornamental horticulture: the case of the rosebush. *Food Qual. Prefer.* **21**, 987–997 (2010)
- Garbez, M., Galopin, G., Sigogne, M., Favre, P., Demotes-Mainard, S., Symoneaux, R.: Assessing the visual aspect of rotating virtual rose bushes by a labeled sorting task. *Food Qual. Prefer.* **40**, 287–295 (2015)



Yann Chéné is a research engineer working on vision systems for agriculture at IMAG PRECISION, Angers, France. He contributed to this work during his Ph.D. research on 3D imaging in plant sciences at Université d'Angers (2011–2014).



Morgan Garbez is a Ph.D. student in biology and agronomy at Agrocampus Ouest, Angers, France. His thesis aims to assess visual characterization tools for ornamental plants with sensory and image analysis methods, together with plant 3D architecture construction over time using the rosebush as model.



David Rousseau is a Professor at Université Lyon 1, France, since 2011, with broad interest and skills in imaging and image processing with applications to life sciences including biology and plant sciences. He headed from 2008 to 2012 the PHENOTIC platform project with Université d'Angers.



Gilles Galopin is an Assistant Professor at Agrocampus Ouest in Angers, France. His research activity is about ornamental horticulture and mainly focuses on the analysis and exploitation of phenotypic plasticity in woody shrubs with ornamental rosebush model.



Étienne Belin is an Assistant Professor at Université d'Angers, France. His research activities are at the interface between information (signal and images) processing and physics, with applications in instrumentation and imaging for plant sciences, via the platform PHENOTIC.



François Chapeau-Blondeau received a Ph.D. in electrical engineering from the University Pierre et Marie Curie, Paris 6, France. He is currently a professor of electronic and information sciences at the University of Angers, France. His research interests include signal processing and imaging, and the interactions between physics and information sciences.